Effect of Secondary Electron Emission on Electron Cross-Field Current in $E \times B$ Discharges

Yevgeny Raitses, Igor D. Kaganovich, Alexander Khrabrov, Dmytro Sydorenko, Nathaniel J. Fisch, and Andrei Smolyakov

Abstract—**This paper reviews and discusses recent experimental, theoretical, and numerical studies of plasma-wall interaction in a weakly collisional magnetized plasma bounded with channel walls made from different materials. A low-pressure $E \times B$ plasma discharge of the Hall thruster was used to characterize the electron current across the magnetic field and its dependence on the applied voltage and the electron-induced secondary electron emission (SEE) from the channel wall. The presence of a depleted anisotropic electron energy distribution function with beams of secondary electrons was predicted to explain the enhancement of the electron cross-field current observed in experiments. Without the SEE, the electron cross-field transport can be reduced from anomalously high to nearly classical collisional level. The suppression of the SEE was achieved using an engineered carbon-velvet material for the channel walls. Both theoretically and experimentally, it is shown that the electron emission from the walls can limit the maximum achievable electric field in the magnetized plasma. With nonemitting walls, the maximum electric field in the thruster can approach a fundamental limit for a quasi-neutral plasma.**

Index Terms—**Cross-field transport, gas discharges, electron kinetics, magnetized plasmas, plasma thrusters, plasma-wall interaction.**

I. INTRODUCTION

MAGNETIZED plasmas can withstand significant steady-state electric fields due to reduced mobility of charged particles across the magnetic field. The control of the electric field in such plasmas has been theoretically and experimentally studied in relation to the basic science of plasma flow in crossed electric and magnetic fields ($E \times B$) and numerous plasma applications such as magnetically confined fusion devices, including tokamaks [1], [2], magnetic mirrors [3], plasma centrifuges [4]–[6], filters for isotope separation and coating applications [7], Large-Area Plasma Device [8], and Hall thrusters [9]–[13].

Fig. 1. Control of the electric field in the $E \times B$ configuration of the Hall-thruster discharge between the anode and the cathode and with the biased segmented electrode [9]–[13].

The most common way to control the electric field in the magnetized plasma is to apply a direct-current (dc) bias voltage $V_b \sim 10$–10^4 V between two or more plasma-facing electrodes, which are electrically and magnetically insulated [2], [4], [8]–[14]. One of these electrodes can be the vacuum chamber [2], [8]. With respect to the magnetic field, the electrodes are placed in such a way that their plasma-facing surfaces are intersected by different magnetic-field lines (see Fig. 1). There are many studies devoted to the question of how the potential gets from the biased electrode to the plasma (see, for example, [1], [14], and [15]). For the floating electrode, the near-wall sheath maintains equal electron and ion fluxes to the wall. When the bias voltage V_b is applied with respect to the plasma, the electrode can drive the current depending on the bias voltage. The sheath screens the plasma from the negative-biased electrode (cathode). For a nonemitting cathode, the potential drop across the sheath can be $\sim V_b$, and the current is carried by ions [14]. For the positive electrode (anode), the sheath screening is much weaker. For low-pressure discharges, the electron-repelling anode sheath (when the anode potential is lower than the plasma potential) has the potential drop on the order of the electron temperature T_e [14], [16], whereas the potential drop of the electron-collecting anode sheath can reach the magnitude of the order of the ionization potential of the working gas [16]. Thus, for the $E \times B$ configuration shown in Fig. 1, the electric potential of the plasma along the magnetic-field lines, which intersect the positive electrode, is near the anode potential. With the increase in the electron emission from the negative electrode, the voltage potential drop across the cathode sheath reduces [16]. As a result, the electric potential of the plasma along the magnetic-field lines, which intersect the negative electrode, can be near the cathode potential. Therefore, the electron emission from the segmented biased electrodes (see Fig. 1) can be used as a valuable tool for controlling the electric field in magnetized plasmas.

The ultimate goal of the electrode biasing is to create and control the electric field in the plasma. This electric field can be used in order to, for example, accelerate the ions and generate the thrust [9]–[13], focus the plasma flow [9], [10], reduce the transport phenomena [1], [2], [8], suppress instabilities [3], [8], improve the plasma confinement [4], and facilitate the mass separation [7]. The conductivity of the plasma along the field lines is stronger than the conductivity across the magnetic field. From Ohm's law, the electric field between the electrodes is inversely proportional to the cross-field conductivity. It is well known that, in many practical implementations of the magnetized plasmas, the cross-field transport is governed by nonclassical mechanisms [8], [14], [17]. These mechanisms can cause the enhancement of the particle and heat transports across the magnetic field, as compared with the classical collisional transport. In turn, the enhanced transport can limit the maximum achievable electric field in the magnetized plasma [13], [18].

In this paper, we consider a weakly collisional plasma in applied electric and magnetic fields, with magnetized electrons and unmagnetized ions. Under such conditions, the electron cross-field current can be driven in the plasma. This current will be carried by ions and electrons. Among various physical mechanisms, which can potentially contribute to the nonclassical electron cross-field transport, scattering electrons on turbulent fluctuations of the electric field is believed to be the most common type (see, for example, [8], [17], and [18]). The resulting anomalous transport, which significantly exceeds the classical values, may exhibit both Bohm $\sim 1/B$ and gyro-Bohm $\sim 1/B^2$ scaling, depending on the regime and experimental conditions [19]. Plasma-wall interaction can also cause the enhancement of the electron cross-field transport [13], [18], [20]–[24]. For example, if the magnetic-field lines intersect a plasma-facing conductive wall, a short-circuit current through this wall can increase the total cross-field current (Simon's effect) [20], [22], [24]. Another example is the so-called near-wall conductivity induced by secondary electron emission (SEE) from the wall. This mechanism was proposed by Morozov and Savelyev [21] to explain the anomalously high electron cross-field current in Hall thrusters. A simplified physical explanation of the near-wall conductivity is as follows. In the presence of a strong SEE from the wall, the voltage potential drop across the plasma-wall sheath decreases. The resulting enhancement of electron-wall collisions leads to the electron cross-field current carried by secondary electrons in the plasma [18], [21], [22], [25]–[27]. The near-wall conductivity scales as the classical collisional transport, i.e., $1/B^2$ [21], which is also similar to the gyro-Bohm turbulent transport. The SEE effect on the electron cross-field current in a Hall thruster is the focus of this paper. The presented results are also relevant to general $E \times B$ plasma flow in various laboratory and applied configurations with electron-emitting walls.

A Hall thruster is a cross-field discharge device, which is used for spacecraft propulsion. In a conventional Hall thruster [the so-called stationary plasma thruster (SPT)], the axial electric and radial magnetic fields are applied in an annular ceramic channel [21]. The thruster plasma is low-pressured and weakly collisional (density of gas atoms $n_a \sim 10^{12}$–10^{13} cm^{-3}; electron plasma density $n_e \sim 10^{11}$–10^{12} cm^{-3}) with $\rho_e \sim$

0.1 cm $< L \sim 1$ cm $\ll \rho_i \sim 10$–100 cm. Here, ρ is the Larmor radius, L is a characteristic size of the plasma, and e and i denote electrons and ions, respectively. The electric field supplies energy mainly to accelerate the ions, but some energy is also spent to heat the electrons, which diffuse across the radial magnetic field. Conventional SPT-type thrusters usually operate with xenon gas. The maximum electron temperature is $T_e \sim 20$–50 eV [26]. This is large enough to cause strong electron-induced SEE from most ceramic materials leading to the near-wall conductivity [21].

The physics of the Hall thruster has been the subject of considerable research efforts, including experimental, theoretical, and numerical studies (see, for example, [21]–[37]). Because the thruster plasma is weakly collisional, kinetic effects are expected to play a key role in virtually all aspects of the thruster operation [21]. In particular, the electron energy distribution function (EEDF) is predicted to depart from the Maxwellian EEDF [21], [26], [29], [33]–[36]. As a result, wall fluxes from the plasma and related processes such as near-wall conductivity, plasma divergence, wall erosion, etc., can be different from predictions of existing fluid theories [26]. This is important because all these processes have direct relevance to the thruster performance and lifetime [22], [25], [27], [30].

Although the importance of kinetic effects in the thruster physics was recognized in the earlier 90s [21], their quantitative description remains a critical challenge. Recent advances in this area have been associated with comprehensive measurements of plasma properties in the thruster discharge [28], [31], [32], the full particle-in-cell (PIC) simulations [33]–[36], and the kinetic modeling [26], [29], [37] of the thruster plasma. In this paper, we review key results of these studies and analyze their implications for Hall thrusters and general $E \times B$ configurations. In this respect, the most remarkable new experimental result is the direct evidence of improved insulation properties of the magnetized plasma where the SEE is suppressed. In particular, it is shown that, without the SEE, the plasma can withstand electric fields that are two to three times larger than it can do in the presence of the SEE. The suppression of the SEE was achieved using an engineered carbon-velvet material for plasma-facing walls of the thruster channel.

This paper is organized as follows: In Section II, we give general considerations on the plasma-wall interaction in the presence of electron emission, including fluid and kinetic descriptions of the SEE effects. We also described the results of kinetic simulations. Here, we focus on the electron-induced SEE from ceramic walls, but the results are relevant to a more general case of a plasma bounded by self-emitting walls, including conductive and dielectric walls. The notion of self-emitting walls implies that the electron emission is induced by the plasma-wall interaction (for example, electron- or ion-induced SEE or self-heating, which maintains thermionic or field emission due to the electric field in the sheath). Section III describes experimental techniques used for studies of plasma-wall interactions in Hall thrusters and reviews experimental results, including the electron cross-field mobility deduced from plasma measurements for different channel-wall materials with different SEE properties. Conclusions and their practical implications are summarized in Section IV.
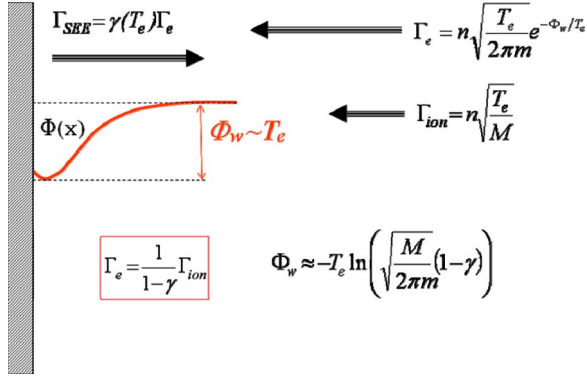
Fig. 2. Effect of the electron emission on the plasma-wall sheath (according to the fluid description of [38]). The voltage drop across the sheath reduces as the SEE coefficient approaches $\gamma_{\rm cr} \approx 1$.

II. THEORETICAL DESCRIPTION OF SEE EFFECTS ON SHEATH AND PLASMA PROPERTIES

A. Fluid Model for the Description of SEE Effects on Sheath and Plasma Properties

It is well-known that the electrons emitted from a surface of the floating wall into the plasma reduce the voltage potential drop in the plasma-wall sheath due to the reduction of the net positive charge in the sheath (see Fig. 2) [38]. In the case of, for example, thermionic emission, the flux of emitted electrons depends on the wall temperature and the work function of the wall material. The electron-induced SEE is a function of the energy of primary electrons from the plasma (or electron beam) and the SEE properties of the wall material. Secondary electrons emitted from a surface are commonly divided into two categories: low-energy "true" secondary electrons with energy of several electronvolts and high-energy inelastically and elastically backscattered electrons with energy in the range of several tens of electronvolts up to the energy of the incident electron [39].

In a quasi-neutral plasma, the electron flux Γ_e to the wall is balanced by the fluxes of ions $\Gamma_{\rm ion}$ and emitted secondary electrons $\Gamma_{\rm SEE}$. This flux balance can be expressed as

$$\Gamma_e = \frac{1}{1 - \gamma(T_e)} \Gamma_{\rm ion} \tag{1}$$

where $\gamma(T_e) \equiv \Gamma_{\rm SEE}/\Gamma_e$ is the averaged SEE coefficient. Fig. 2 illustrates the SEE effect on the plasma-wall sheath according to [38], under the assumption of a Maxwellian EEDF. When the flux of secondary electrons from the wall approaches the flux of primary electrons from the plasma, i.e., $\gamma(T_e) = \gamma_{\rm cr} \approx 1$, the sheath becomes space-charge saturated (SCS). Any further increase in the secondary electron flux into the plasma is restricted by a potential minimum formed near the wall surface.

Under conditions of the SCS sheath (see Fig. 2), the plasma potential with respect to the wall is reduced to nearly $\Phi_w \sim T_e$, as compared with several times of T_e without the SEE (for example, for xenon, $\Phi_w \approx 5.77 T_e$ without the SEE [40]), and the electron flux to the wall [see (1)] is considerably larger than the electron flux without the SEE. As a result, the wall acts as

an extremely effective energy sink [14]

$$q_e \approx \left(\frac{2T_e}{1 - \gamma(T_e)} + e|\Phi_w| \right) \Gamma_{\rm ion} \tag{2}$$

where q_e is the electron power flux density removed from the plasma. Equation (2) accounts for the fact that only electrons with energies of $\geq e|\Phi_w|$ will reach the wall. This is without taking into account electron energy losses in the presheath and the energy returned to the plasma with secondary electrons. For example, for the xenon plasma, the SCS regime occurs when the SEE coefficient approaches its critical value $\gamma_{\rm cr} = 1 - 8.3 \cdot (m/M)^{0.5} \approx 0.983$ [38]. Here, m and M are the electron mass and ion mass, respectively. For the plasma bounded with ceramic walls made from, for example, a boron nitride ceramic, the critical SEE is achieved when the electron temperature $T_e \approx 18$ eV [41]. According to the fluid models of the Hall thruster [22], [25], [27], because of the SCS sheath regime, the maximum electron temperature should not exceed this critical temperature.

Finally, for Hall thrusters and similar $E \times B$ discharges, the SCS sheath regime can have another important implication. According to [22] and [27], the effective electron-wall collision frequency in the thruster channel drastically increases when the sheath is SCS, i.e.,

$$v_{ew} \equiv \frac{\Gamma_e}{n_e H} \approx \frac{1}{n_e H} \frac{\Gamma_{\rm ion}}{1 - \gamma(T_e)} \tag{3}$$

where H is the distance between the channel walls and height. This leads to the enhancement of the electron cross-field conductivity (near-wall conductivity [21]).

B. Kinetic Treatment of SEE Effects on Sheath and Plasma Properties

For collisionless and weakly collisional plasmas, where the electron mean free path $\lambda_{\rm em}$ is larger than the characteristic size of the plasma, the assumption of the Maxwellian EEDF cannot be justified. Indeed, energetic electrons should quickly escape from the plasma to the wall. Depending on their energy at the wall, these electrons can be either lost due to a wall recombination with ions or liberate SEE electrons from the wall. In the absence of sufficient electron–electron collisions in the plasma, there is no obvious mechanism to maintain the Maxwellian EEDF. Under such conditions, the resulting EEDF is depleted at high energies due to wall losses. Because $\lambda_m > H$, the electron losses to the walls can be hundreds of times smaller than the losses predicted by the fluid theories [see Fig. 2 and (1)–(3)] [26]. A similar depletion of the electron velocity distribution function (EVDF) at high energies was also reported for other kinds of low-pressure discharges [42], [43].

Another important aspect of low collisionality in low-pressure plasmas is that the electron–atom and electron–ion collisions are not frequent enough to isotropize the EVDF. Therefore, the depletion of energetic electrons in the velocity phase space is expected to occur mainly in the direction toward the wall. As a result, the EVDF can become anisotropic [26], [33].
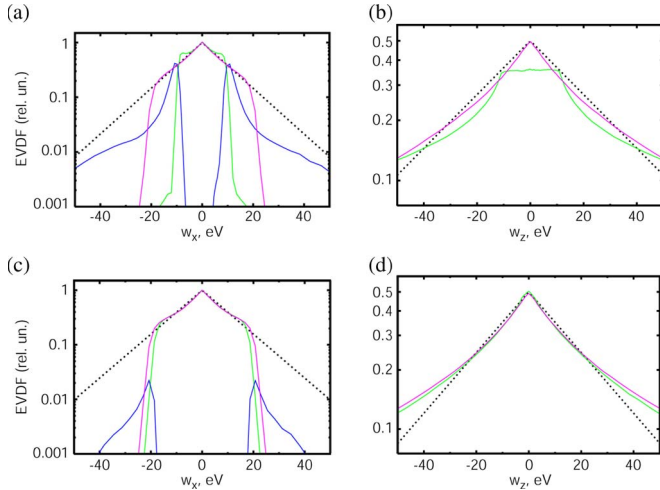
Fig. 3. Results of Particle-in-Cell simulations for $E \times B$ plasma slab bounded between two walls. The simulations were conducted using a full 1-D 3-V PIC code [26. 33–35]. The electron velocity distribution function (EVDF) along and across the magnetic field ($B = 100$ Gauss): (a) and (b) for $E = 200$ V/cm, and (c) and (d) for $E = 100$ V/cm. In addition, the following input parameters were used for these simulations: the neutral density of $1 \cdot 10^{13}$ cm^{-3}, the effective anomalous collision frequency of $2.8 \cdot 10^6$s^{-1}. The simulated plasma density is $2.7 \cdot 10^{11}$ cm^{-3} for (a) and (b) and $4.3 \cdot 10^{11}$ cm^{-3} for (c) and (d). The EVDF is compared for plasmas with and without secondary electron emission: (a) and (c) in the X-direction normal to the wall and parallel to the magnetic field, and (b) and (d) in the Z-direction parallel to the wall and the electric field. The EVDF's of the bulk plasma with and without SEE are shown with green and magenta lines, respectively. The EVDF of counterstreaming SEE beams is shown with blue lines. For comparison, the Maxwellian EVDF is shown for each direction with dashed black lines (for $E = 200$ V/cm, $T_{ex} = 10.4$ eV and $T_{ez} = 32.3$ eV; and for $E = 100$ V/cm, $T_{ex} = 10.8$ eV and $T_{ez} = 28.1$ eV). The main results are: 1) the EVDF over the velocity normal to the wall is depleted in the high-energy tail due to loss of fast electrons at the walls; 2) EVDF over the velocity parallel to the wall is not depleted due to rare collisions which scatter electrons to the loss cone; 3) with SEE, there are counterstreaming beams of secondary electrons propagating between two opposite walls; 4) strong SEE effects occur when the beam energy is large enough to sustain the counterstreaming beams. The latter requires a strong electric field in the plasma (≥ 200 V/cm).

In [33]–[35], a full 1-D 3-V PIC code was used to study the EVDF and SEE effects in the weakly collisional magnetized plasma of the Hall thruster ($H = 2.5$–3 cm, $n_e \sim 10^{11}$–10^{12} cm^{-3}, $n_a \sim 10^{12}$–10^{13} cm^{-3}, and $E \sim 10^2$ V/cm and $B \sim 10^2$ G). Illustrative results of PIC simulations using this code for the EVDF with and without the SEE are shown in Fig. 3. Compared with previous simulations [26], [33]–[35], these results were obtained using improved analytical approximations for differential cross sections for scattering electrons in electron-neutral elastic collisions described in the Appendix. The simulations considered the electric field in the range of 50–200 V/cm and predicted the effective electron temperatures of 20–40 eV and 10–12 eV in the direction parallel and perpendicular to the wall, respectively. In addition to numerical simulations, in [26], analytical expressions were developed to characterize the effects of low plasma collisionality on the plasma-wall interaction. The flux of plasma electrons to the wall is predicted to be $H/2\lambda_m$ times smaller, as compared with Γ_e for the Maxwellian EVDF. This factor accounts for the depleted loss cone of the velocity space in the direction toward the wall.
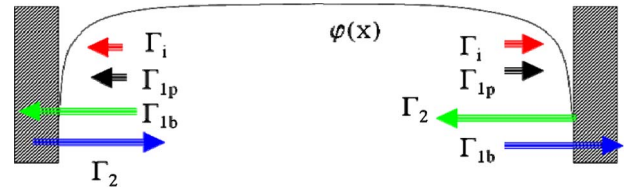
Fig. 4. Plasma-wall interaction in a weakly collisional magnetized plasma bounded between two emitting walls [26], [33], [37], [45], [46]. Γ_i is the ion flux from the plasma to the wall. Γ_{1p} is the flux of plasma electrons to the walls scattered by collisions with neutral and plasma particles. Γ_2 is the beam of secondary electrons departing from the wall. Γ_{1b} is the beam of secondary electrons arriving to one wall from the opposite walls. The plasma potential profile between the walls is also shown.

Note that we use here the term loss cone to describe the area in the velocity phase space, which contains particles with the energy of motion normal to the walls sufficient to penetrate through the potential barrier of the sheath [33].

Because of the reduced electron flux to the wall, the plasma potential with respect to the wall is also reduced, as compared with the plasma case with the Maxwellian EEDF $\sim \Phi_w - T_e \ln(\lambda_m/H)$. Here, for the plasma with the non-Maxwellian EVDF shown in Fig. 3, T_e is the effective electron temperature [26], [33]. For example, for the Hall thruster, PIC simulations predicted a plasma potential of 20–28 V, with $\Phi_w \sim T_e$ [26]. This is significantly smaller than the plasma potential estimated for the Maxwellian EEDF and xenon without electron emission, with $\Phi_w \approx 5.77 T_e$ [40].

Because the EVDF is not depleted in the direction of the electric field parallel to the wall, [see Fig. 3(b) and (d)], high-energy electrons with energy above the plasma potential Φ_w are preserved in the plasma. The flux of these electrons to the wall is controlled by rare collisions with heavy particles (for the thruster plasma, the loss cone is mainly formed by collisions with atoms) [26]. When there is no SEE (no backscattering and no true secondary electrons), the plasma electrons will be lost due to recombination at the wall. Fig. 3(a) (magenta curve) shows the EVDF for such an electron-absorbing wall. In the presence of the SEE from the wall (green curves for bulk electrons in Fig. 3), secondary electrons are accelerated in the sheath toward the plasma and form the beam [blue curves in Fig. 3(a) and (c)] [33]. According to PIC simulations [33], [34], the SEE beam from one wall can reach the opposite wall without being strongly affected by collisions with the other particles in the plasma or various plasma instabilities such as two-stream instability between beam of secondary electrons and plasma electrons. This situation with SEE beams unaffected by the two-stream instability is similar to other low-pressure magnetized plasma such as in the expansion tank of the magnetic mirror [44] and dc magnetron discharges.

Consider counterstreaming beams of secondary electrons between two opposite walls with symmetrical sheaths (see Fig. 4). After gaining the energy due to the acceleration in the sheath at one wall, the beam electrons lose their kinetic energy while crossing the sheath at the opposite walls. If the electron incident energy is low (< 5 eV), there is a probability for electron backscattering to occur [22], [33], [39]. However, the SEE due to the backscattering process from metals and ceramics is always smaller than $\gamma_{cr} \approx 1$ [22], [41]. A different
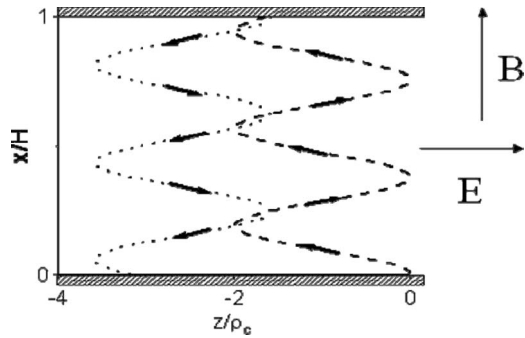
Fig. 5. Schematic of the near-wall conductivity in crossed electric and magnetic fields due to the counterstreaming beams of secondary electrons [26].

TABLE I
EFFECT OF THE ELECTRIC FIELD ON THE NEAR-WALL CONDUCTIVITY
INDUCED BY SEE BEAMS. γ_p AND γ_b ARE PARTIAL SEE COEFFICIENTS
DUE TO PLASMA AND BEAM ELECTRONS, RESPECTIVELY.
γ_T IS THE TOTAL SEE COEFFICIENT [45]

E, V/cm	γ_p	γ_b	γ_T	$J_{NW}/J_{e\perp}$
100	1.5	0.69	0.83	≤ 0.05
140	1.65	0.82	0.9	0.25
200	1.54	0.97	0.978	0.64

situation can take place for the $E \times B$ configurations such as shown in Fig. 5. Here, the beam electrons gain an additional energy due to the $E \times B$ motion. The energy of the beam electron at the moment of its collision with the wall is [45]

$$\varepsilon_B = mV_{\mathrm{dr}}^2 (1 - \cos \varphi) \qquad (4)$$

where $V_{\mathrm{dr}} = E/B$ is the drift velocity in the crossed electric and magnetic fields, and $\varphi = \omega_{\mathrm{ce}}\tau$ is the final phase of cyclotron rotation before the electron collides with the wall. Here, $\omega_{\mathrm{ce}} = eB/m$ is the electron gyrofrequency, and τ is the electron time of flight between the wall.

Note that the maximum of the additional electron energy on a scale of the gyroradius (see Fig. 5) is

$$\varepsilon_{B\,\mathrm{max}} = 2eE\rho_e. \qquad (5)$$

If this energy is insufficient to induce a strong SEE, counterstreaming beams of emitted electrons will have a weak effect on the plasma. Fig. 3 shows the simulated results for $E = 100$ and 200 V/cm. In addition, Table I summarizes the SEE yields for plasma and beam electrons. With the increase in the electric field, the beam-induced SEE γ_b also increases. For $E = 200$ V/cm and $\rho_e \approx 0.15$ cm, the maximum possible beam energy [see (5)] $\epsilon_{B\,\mathrm{max}} \approx 60$ eV. According to (4) and [45], this is large enough to ensure that beams induce $\gamma \approx \gamma_{\mathrm{cr}}$ from a boron nitride ceramic [41], i.e., the material of the thruster channel walls. A detailed analysis of the simulated results for the EVDF in the thruster plasma and its dependence on the input parameters, including the electric field, the effective frequency of turbulent collisions, and the channel height, is described elsewhere [26], [33]–[35], [45], [46].

Note that, in the case of symmetrical sheaths on both walls and the strong SEE from these walls, the contribution of the arriving and departing beams to the total current balance on each wall is canceled [26], [37]. Under such conditions, the sheath

potential between the floating emissive wall and the plasma is determined by the balance between the ion and electron fluxes from the plasma (loss cone) [26]. This is equivalent to the case of the plasma-wall sheath in the absence of the electron emission.

C. Kinetic Treatment of SEE Effects on the SEE-Induced Electron Cross-Field Current

For the Hall thruster and similar $E \times B$ configurations, the counterstreaming SEE beams can induce the enhancement of the electron cross-field current (near-wall conductivity [21]) [26], [33], [46]. This occurs because a secondary electron during one pass from one wall to the opposite wall moves across the magnetic field toward the anode by the distance of the order of the electron gyroradius (see Fig. 5). According to [26] and [46], the axial electron current density due to the beams of SEE electrons (near-wall conductivity) is

$$J_{\mathrm{NW}} \propto \frac{1}{H} \frac{\gamma_p}{1 - \gamma_b} n_e \sqrt{\frac{T_{e\perp}}{M_i}} \frac{E_\perp}{B^2} \qquad (6)$$

where γ_p and γ_b are the partial SEE coefficients for the plasma and beam electrons, respectively. Because the near-wall conductivity is carried by the SEE beams, its contribution to the electron cross-field current increases with the beam energy [see (4) and (5)] and becomes the dominant mechanism of the cross-field current in the thruster when γ_b approaches 1 (see Table I).

According to (4) and (5), the beam energy is determined by the strength of the electric field, which depends on the discharge voltage V_d. Changes of the magnetic field, which can affect the electric field, can also be accompanied with changes of the maximum beam energy [see (5)]. In addition, the distance between the channel walls can have a nonmonotonic effect on the final phase of the cyclotron rotation φ [45] and, thereby, on the incident energy and the incident angle of beam electrons at the wall. Simulations predict that, with all input parameters the same, the reduction of the electric field causes an abrupt reduction of the near-wall conductivity (see Table I).

When the density of neutral atoms near the wall has a local peak due to, for example, recombination at the wall or outgassing from the wall during the plasma discharge, collisions of secondary electrons with atoms can additionally enhance the near-wall conductivity [47]. Moreover, a high-frequency sheath instability, which is predicted to occur in the SCS regime, may also contribute to the enhancement of the electron cross-field transport [36]. This instability occurs due to a negative differential resistance of the sheath near the emitting wall [35], [36].

Note that there are a number of other factors that can alter the SEE effect on the plasma-wall interaction and the near-wall conductivity. For example, the cylindrical geometry and 2-D topology of the magnetic field, including the oblique magnetic field with respect to the emitting wall, can alter the SEE [18], [48] asymmetrical sheath conditions on the opposite channel walls [36]. This may change the total current balance at the walls. In Section III, we compare wall-material effects on the thruster operation with the same magnetic-field topology and the channel geometry.

III. EXPERIMENTAL DEMONSTRATION OF SEE EFFECTS ON PLASMA PROPERTIES AND THE ELECTRON CROSS-FIELD CURRENT

A. Materials for Nonemitting (Absorbing) and Emitting Walls

There is a reliable experimental evidence that the Hall-thruster operation is very sensitive to the wall material of the thruster channel [13], [22], [49]–[51]. Conventional Hall thrusters use a boron nitride ceramic as the channel-wall material [21], [22], [50]. Several studies pointed to the existence of a correlation between the discharge current and the SEE properties of the ceramic-wall materials [22], [49], [50]. In particular, for constant discharge voltage and magnetic field, larger values of the discharge current were measured for ceramic materials with lower values of the energy threshold for the SCS. However, for most of ceramic materials applicable for thruster applications, this energy threshold is in the range of 30–40 eV [41]. This is comparable with measurement uncertainties of the electron temperature and the plasma potential for the probe diagnostics used in [31] and [51]. Therefore, it is not so obvious that the observed differences in the thruster operation with different ceramic-wall materials of the thruster channel can be attributed to differences in the SEE properties of these materials.

Note that, during the thruster operation, surface properties of the ceramic walls, including the SEE, may be affected by outgassing [52], physical and chemical sputtering, and deposition of various coatings and high temperatures ($\sim$1000 °C). There is no published data on the SEE yield from ceramic materials after and during their exposure to the plasma. This can also complicate a validation of theoretical predictions of the SEE effects in the thruster discharge.

In a number of thruster studies, the channel walls were made from metal and graphite materials [13], [22], [23], [32], [49]–[51], [53], [54]. For typical electron temperatures in the thruster discharge (20–50 eV), these materials have much lower SEE than ceramic materials. For example, for graphite-type materials, even the maximum SEE yield (at the energy of primary electrons of 300 eV) may not reach the critical yield for the SCS sheath with xenon gas ($\gamma_{cr} \approx 0.983$). With a smaller SEE, the electron cross-field current is expected to be smaller [see Table I and (4)]. However, the short-circuit current through the conductive wall made from metal or graphite materials can increase the discharge current [22], [23], [50].

In the absence of the electron emission from the conductive wall, the short-circuit current is determined by the ion flux to the wall and the ion-collecting area [22], [23]. For a typical SPT-type Hall thruster, the length of the annular channel measured between the anode and the channel exit can be several centimeters. When the channel walls are entirely made from metal or graphite materials, the resulting discharge current can be larger than the discharge current for the thruster with ceramic walls [22], [50]. This is partially because the ion flux from the plasma is collected by the entire channel. The reduction of the ion-collecting area can reduce the short-circuit current [22], [23]. All critical plasma parameters of the thruster discharge, including the electric field and the elec-
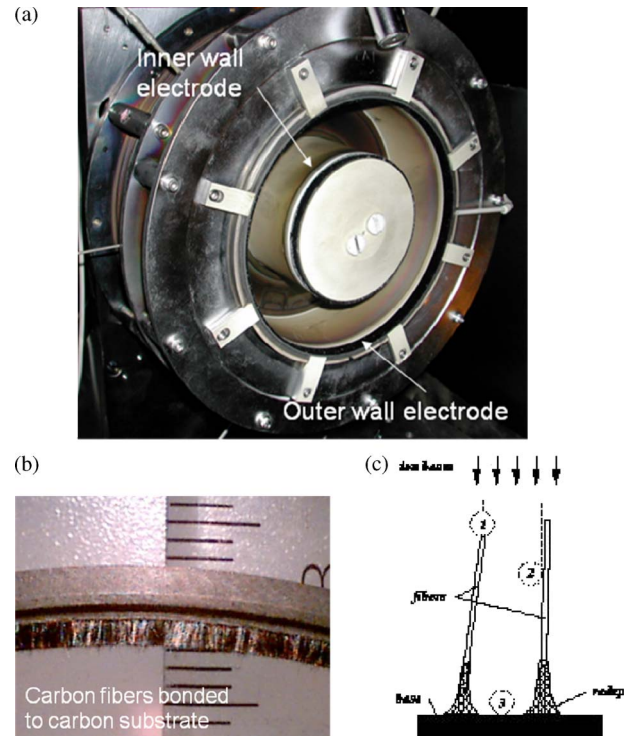
Fig. 6. Two-kilowatt segmented-electrode Hall thruster: (a) narrow segmented electrodes are placed at the exit of the 12-cm-outer-diameter thruster channel made from a boron nitride ceramic material. (b) The segmented electrodes are made from a sputter-resistant carbon-velvet material to suppress the SEE [53]. (c) Schematic of the velvet material (courtesy of the Energy Science Laboratories, Inc., http://www.esli.com). In the thruster operation, the electrodes can be floating or biased with respect to the cathode.

tron temperature, reach their local maxima within a region of $\sim$0.5–1 cm from the channel exit inside the thruster channel [13], [31], [55]–[57]. Therefore, it was sufficient to place short-length segments made from low SEE and low sputtering conductive materials in this region in order to affect the thruster plasma without a large short-circuit current [13], [23], [32], [53], [54].

Fig. 6 shows a 2-kW laboratory Hall thruster with two approximately 1-cm-length conductive segments placed on the inner and outer walls of the boron nitride ceramic channel [32], [53]. The channel outer diameter is 12 cm, $H = 2.5$ cm, and the channel length L is 4.6 cm. Because both segments can be floating or biased, we shall refer to them as segmented electrodes. These segmented electrodes were made from a graphite velvet material [53]. The sputter resistance of this engineered metamaterial is exceptionally good, particularly with respect to the backflow of contamination. This is because ions strike the velvet at grazing incidence and sputtered particles get trapped in the velvet texture [see Fig. 6(c)]. An important feature of the carbon velvet is that, because of interfiber cavities with a large aspect ratio of $\sim$10^2, it is expected to suppress both ion- and electron-induced SEEs from the electrode [32]. In addition, the graphite velvet allows minimizing the backflow of atoms that resulted from recombination at the wall. Thus, the use of the graphite velvet material offers a unique opportunity to achieve the operation of the Hall thruster without the SEE-induced near-wall conductivity.

B. Remarks on Probe Measurement Procedures

In the described experiments, plasma properties, including plasma potential and electron temperature, were measured using various movable and stationary electrostatic probe techniques, including emissive probes and biased collecting probes. A detail description of the probes, the measurement procedures used in these experiments, the analysis of measurement uncertainties, and the probe-induced perturbations of the plasma are given in [31], [58], and [59]. The electric field was deduced from measurements of the floating potential using a movable emissive probe. This probe was heated by an external floating power supply to operate at the limit of a strong electron emission. The emissive probe measurements were corrected to account for space-charge effects [31]. The standard deviation of these measurements was in the range of $\pm 5\%$–15%. The electron temperature was deduced from floating potential measurements of movable hot emissive and cold probes. The assumption of the Maxwellian EEDF was applied [31]. Uncertainties in the determination of the electron temperature due to the orbital-motion-limited effects were in the range of $\pm 17\%$ [31].

Note that a procedure using nonbiased movable probes has many advantages for measurements in harsh environments of a Hall-thruster plasma. However, the assumption of the Maxwellian EEDF can introduce an uncertainty in the determination of the electron temperature. Nevertheless, a comparison with other probe techniques (e.g., biased Langmuir probe) suggested that the applied measurement procedure did give an approximate value of the mean electron energy in the thruster plasma [31].

In addition, according to predictions of the PIC simulations (see Fig. 3), the electron distribution function over velocities parallel to the walls is not depleted. The flux of electrons with an energy above some threshold in this direction is larger than the corresponding flux along the magnetic-field lines. The ratio of these fluxes is about the square root of the ratio of electron temperatures parallel and normal to the walls if the threshold is below the plasma potential with respect to the wall (the energy where the depletion of the electron distribution over the velocities normal to the wall begins). In our PIC simulations (see Fig. 3 and [33]–[35]), the ratio of temperatures was usually about 3. Hence, the ratio of fluxes is about 1.7 for electron energies below the plasma potential with respect to the wall. If the aforementioned threshold is above the plasma potential, this ratio can be much larger. For example, for the case with the electric field $E = 140$ V/cm (see Table I), the flux ratio is about 2.5 times. Thus, in our probe measurements, the contribution of the electron flux parallel to the walls is predicted to be dominant over the electron flux along the magnetic-field lines. It may imply that the temperature deduced from these measurements is approximately the effective electron temperature perpendicular to the magnetic field T_{ez}. This is relevant to all thruster regimes in which the electron $E \times B$ drift velocity V_{dr} is sufficiently smaller than the electron thermal velocity V_{th}. As shown in Section III-C, there are high-discharge-voltage regimes of the thruster with nonemitting walls for which $V_{\mathrm{dr}} \geq V_{\mathrm{th}}$.
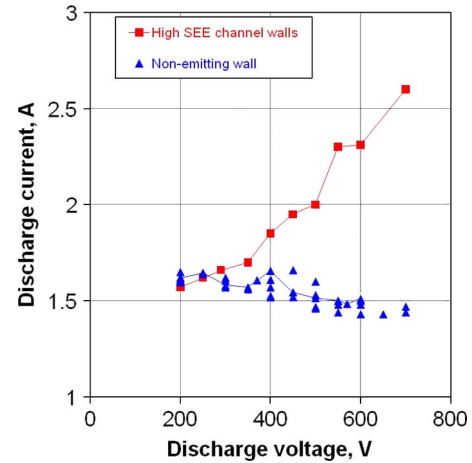
Fig. 7. Comparison of the V–I characteristics for the high SEE boron nitride ceramic walls and the nonemitting carbon-velvet walls (floating segmented electrodes on outer and inner channel walls; see Fig. 6) [32], [53]. The magnetic field and the gas flow rate are constant for all thruster regimes.

Finally, while comparing the measured and simulated electron temperatures, it is important to know how the electron temperature is defined for a non-Maxwellian EVDF. In our simulations, T_e has been defined as the energy value at which the distribution falls of by e^{-1} from its maximum at $w = 0$ (Fig. 3). If T_e is estimated instead based on the predicted mean electron energy, then for these, strongly anisotropic EVDFs, T_{ez} would be twice the mean energy of the v_z distribution (parallel to the walls and in the direction of the electric field). For example, for the simulated case with $E = 200$ V/cm [Fig. 3(a) and (b)] it is about 60 eV. The temperature T_{ex} would equal the mean energy of the v_x distribution (in the direction normal to the walls and along the magnetic field), which is about 10 eV.

C. Measurements of SEE Effects on Sheath and Plasma Properties

The thruster operation with high SEE boron nitride ceramic walls and nonemitting graphite velvet electrodes is getting remarkably different as the discharge voltage increases above a certain voltage threshold (~ 400 V; see Fig. 7). In particular, with high SEE walls, the discharge current becomes much larger than that with the nonemitting walls. This current increase is mainly due to the increase in the electron cross-field current [32]. The electron current $I_{e\perp} = I_d - I_i$ was obtained from measurements of the discharge current I_d and the total ion current in the plasma plume I_i.

Note that the change of the electrode potential from floating to cathode biased did not produce a significant effect on the V–I characteristic [32], [53]. The measured current through the cathode-biased electrode was less than 10% of the discharge current and almost did not change with the discharge voltage. The negative-biased electrode collects the ion flux from the plasma. The collected current by this electrode is also nearly equal to the short-circuit current through the floating conductive electrode [23]. Apparently, for the segmented-electrode Hall thruster, the short-circuit current accounts for a relatively small fraction of the total cross-field current.
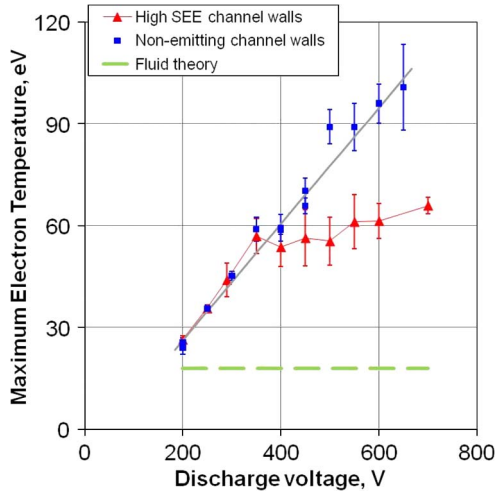
Fig. 8. Comparison of the measured maximum electron temperature as a function of the discharge voltage for the high SEE boron nitride ceramic walls and the nonemitting carbon-velvet walls (floating segmented electrodes on outer and inner channel walls; see Fig. 6) [32]. The discharge voltage controls the Joule heating of electrons. (Dashed green curve) Maximum temperature in the channel estimated according to the fluid theory of [38]. The magnetic field and the gas flow rate are constant for all discharge-voltage regimes.

Fig. 8 shows how the maximum electron temperature inside the thruster depends on the discharge voltage. These results were discussed and analyzed in detail in [31], [32], and [57]. The discharge voltage controls the Joule heating in the thruster discharge. For both channel-wall materials, where a linear increase in the maximum temperature with the discharge voltage exists, the wall-material effects are minor in these regimes. The temperature saturation observed for the ceramic-channel case was attributed to the SEE effect [31].

The fact that the electron temperature at saturation is higher than that predicted by fluid theories [13], [22], [27], [60] suggests that understanding the Hall-thruster plasma in detail requires a kinetic treatment [26]. In particular, it may suggest the presence of a depleted anisotropic EEDF with beams of secondary electrons leading to the near-wall conductivity [26], [33]–[35], [45], [46]. This could explain the increase in the electron cross-field current with the discharge voltage observed for the high SEE case (see Fig. 7).

Fig. 9 demonstrates the axial electric-field distribution measured for the cases of the high SEE and nonemitting channel walls. The electric field was obtained by differentiating the measured plasma potential distribution along the channel median [31]. The following most significant differences between these two cases are observed at high discharge voltages: 1) With nonemitting walls, the electric field can be two to three times larger than that with high SEE walls. In the latter case, the increase of the discharge voltage causes the potential drop to occur along the longer region. This region extends inside the ceramic channel and in the plasma plume [31], [40]. 2) With high SEE walls, the maximum electric field shifts to the near-plume region away from the channel [see Fig. 9(a)]. This is not the case for the nonemitting walls [see Fig. 9(b)]. Here, even at high discharge voltages, the maximum electric field remains inside the channel in the region of a strong magnetic field.

For high SEE walls, the observed changes of the electric-field distribution with the discharge voltage [see Fig. 9(a)]
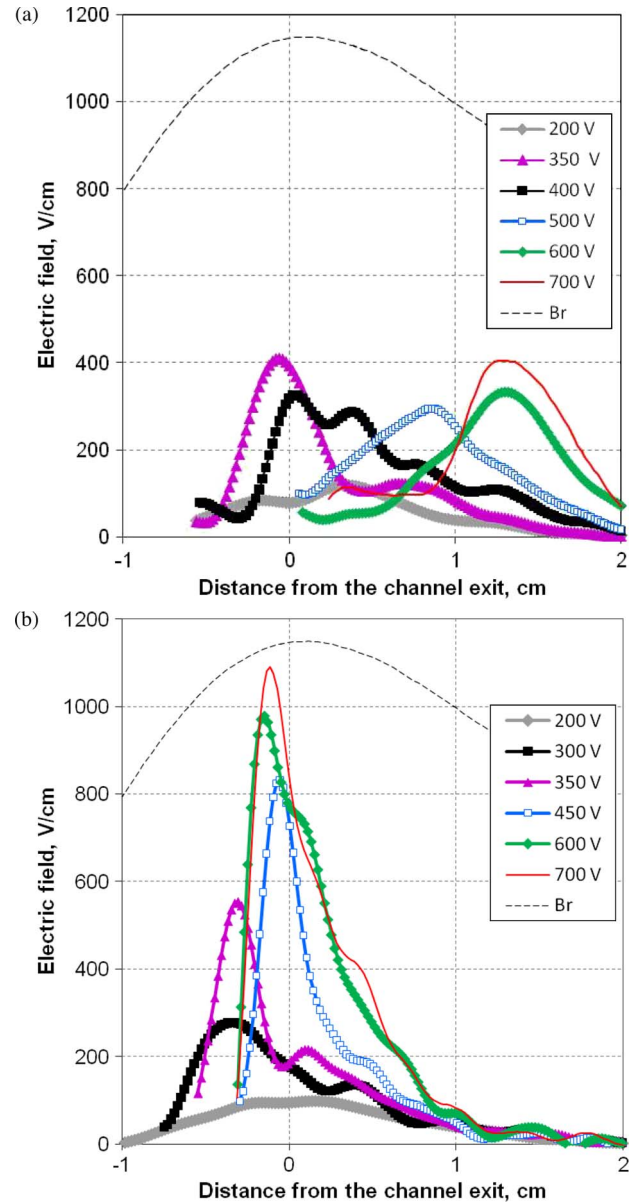
Fig. 9. Electric field along the thruster channel median obtained (a) for the high SEE channel made from the boron nitride ceramic and (b) for the segmented thruster with nonemitting floating walls (segmented electrodes) made from the carbon-velvet material (see Fig. 6). The anode position inside the thruster channel is at the distance of −4.6 cm from the channel exit. The magnetic field and the gas flow rate are constant for all discharge-voltage regimes. The profile of the radial magnetic field is also shown with the maximum magnetic field $B_{rmax} = 115$ G. The electric field was obtained by differentiating the measured plasma potential distribution along the channel median. Note that, (top) for the high-SEE-channel case, the fast movable probe, which was used for plasma potential measurements, induced strong plasma perturbations at high discharge voltages [31]. For the probe measurements inside the channel, where probe-induced perturbations of the plasma were particularly strong, the electric field is not shown.

can be explained by the enhancement of the electron cross-field current inside the high SEE channel [13] and [40]. The near-wall conductivity seems to be the mechanism most likely responsible for this enhancement. With a constant discharge voltage, the SEE-induced near-wall conductivity causes a larger fraction of the voltage potential drop to be placed outside the channel [13], [31], [40], [51], [60]. Here, the maximum electric field reaches its local maximum.

For the high-discharge-voltage operation without the SEE, the electric field inside the channel can be strong [$\sim 10^3$ V/cm at $V_d > 600$ V; see Fig. 9(b)], whereas with the SEE, the maximum electric field inside the channel does not exceed ~ 100 V/cm at $V_d > 400$ V [see Fig. 9(a)]. For $E = 100$ V/cm and $\rho_e = 0.15$ cm, $\epsilon_{B\,\mathrm{max}} \approx 30$ eV [see (5)] is just enough to get $\gamma(\epsilon) \approx 1$ from boron nitride [41]. According to [45], $\varphi \neq \pi/2$ [see (4)]. Thus, the beam energy at $E = 100$ V/cm seems to be not enough to sustain strong beams of secondary electrons. Among possible explanations of this discrepancy between predictions of PIC simulations and the experiment, we can mention probe-induced perturbations of the plasma inside the channel [31], [58], limitations of the 1-D code, and possible time-dependent processes in the thruster (e.g., oscillations of the electric field [28], [36]), which were not captured by steady-state measurements in the described experiments.

Without specifying the exact mechanism of the electron transport, we shall compare the electron cross-field mobility $\mu_\perp = e\nu_e/m_e\omega_{\mathrm{ec}}^2$ for the cases of the high SEE and nonemitting walls. The mobility can be deduced by substituting measured plasma parameters into 1-D Ohm's law, i.e.,

$$v_{\mathrm{ez}} = \mu_\perp \left[E - (1/en_e)d(n_e T_e)/dz\right]. \tag{7}$$

The electron velocity was estimated using the measured plasma and discharge parameters $v_{\mathrm{ez}} = I_{e\perp}/en_e A$, where A is the plasma cross section (in the channel or in the plume deduced from the measured plume divergence angle). The mobility varies along the thruster channel because of the nonuniform magnetic field and the variations of the electron collision frequency ν_e. Fig. 10 compares the experimental electron mobility, which was obtained at the local maximum of the electric field, as a function of the discharge voltage. In addition, the classical mobility estimated for electron–atom collisions is also shown in Fig. 10. The atom density was assumed to be $5 \cdot 10^{12}$ cm^{-3}, which is typical for Hall thrusters. For each discharge voltage, the electron temperature measured for the thruster with nonemitting walls was used for the estimation of the classical mobility. For both channel wall materials cases, the experimental mobility appears to be larger than the classical one.

When the SEE has no effect on the thruster plasma (below the discharge voltage of 400 V—for high SEE channel walls, the voltage threshold for the dependence of the maximum T_e on V_d), the mobility trends are not so sensitive to the wall material. In the absence of the near-wall conductivity, the enhanced electron conductivity may be caused by the anomalous fluctuation-induced mechanism. It is indeed surprising that, for both wall-material cases, the mobility tends to decrease as the discharge voltage (and the electric field) increases to the discharge voltage of 350 V. This mobility reduction with the discharge voltage is not understood at the moment. A shear-based mechanism of the reduction of the electron transport in the Hall-thruster discharge has been proposed in [61] and developed in [62] within a semiempirical analysis and without the identification of the mode(s) responsible for the anomalous transport.
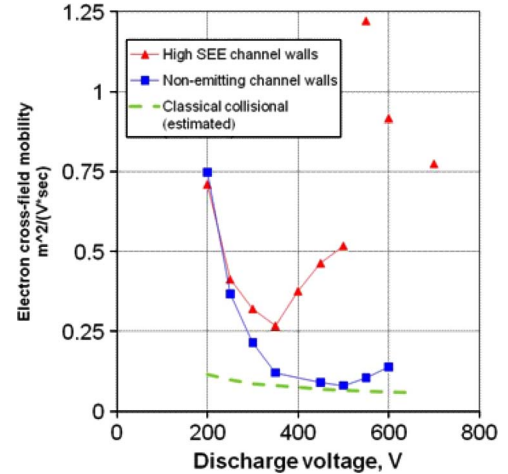
Fig. 10. Comparison of the electron cross-field mobility with the classical mobility for the high SEE boron nitride walls and the nonemitting carbon-velvet walls (floating segmented electrodes on the outer and inner walls of the channel; see Fig. 6). The experimental mobility was deduced from measurements at the local maximum of the electric field. (Dashed green curve) The classical mobility was estimated under the assumption of dominant electron–atom collisions at $n_a = 5 \cdot 10^{12}$ cm^{-3} and using T_e measured for the thruster with nonemitting walls.

The $E \times B$ shear could be possibly responsible for the reduction of the mobility with the discharge voltage observed in this paper (see Fig. 10). The shear of the $E \times B$ velocity along the channel becomes larger with the increase in the maximum electric field at a constant magnetic field (see Fig. 9). This is particularly relevant for the thruster with nonemitting walls. For this thruster, a simplified calculation of the shearing frequency, i.e., $d(E_z/B_r)/dz$, suggests that it increases from 0.15 ns^{-1} at 200 V to 5–8 ns^{-1} at 600 V. With high SEE walls, the shearing frequency reaches its maximum of about 1 ns^{-1} at 350–400 V and then drops at higher discharge voltages. A large shear of the electric field may affect the dynamics of instabilities, which were predicted and some of which were measured for conventional Hall thrusters at a moderate discharge voltage [21], [28], [63]–[65]. Furthermore, the large shear of the electric field, which may exist in the thruster with nonemitting walls, may lead to the occurrence of specific kinetic regimes [35], [46].

At high discharge voltages, the mobility increases for high SEE walls but continues to drop for low SEE walls. The former result can be attributed to the SEE-induced near-wall conductivity. Within the accuracy of the probe measurements [31], the electron cross-field transport in the channel with low SEE walls is suppressed to almost a classical level. Apparently, with nonemitting walls, it is possible to significantly improve insulation properties of the magnetized plasma at high discharge voltages, as compared with the plasma bounded with high SEE walls. With such improved insulation, the maximum electric field measured at > 600 V ($\sim 10^3$ V/cm) is just a few times below a fundamental limit for a quasi-neutral plasma, i.e., $E \sim T_e/\lambda_D$ (for $T_e \sim 100$ eV and $n_e \sim 10^{11}$ cm^{-3}), where λ_D is the Debye length. Moreover, in these regimes, the $E \times B$ rotation of electrons becomes supersonic (for example, at $V_d = 600$ V, the ratio of the drift-to-thermal-electron velocities at the placement of the local maximum of the electric field along the thruster channel is $V_{\mathrm{dr}}^{\mathrm{max}}/V_{\mathrm{th}}^{\mathrm{max}} > 2$). This may lead to kinetic

effects on the plasma potential distribution due to increased centrifugal forces on electrons [66].

IV. Concluding Remarks

The purpose of this paper has been to review recent experimental, theoretical, and numerical studies of the plasma-wall interaction in Hall thrusters and discuss their implications for the control of the electric field in $E \times B$ discharges. The presence of a depleted anisotropic EEDF with beams of secondary electrons emitted from the thruster channel walls has been predicted to explain the enhancement of the electron cross-field current observed in experiments. These results support the existence of the SEE-induced near-wall conductivity in the conventional Hall thruster with high SEE ceramic walls (SPT-type) [21].

The contribution of the near-wall conductivity to the electron cross-field current increases with the electric field. This implies that the electron emission from the walls can limit the maximum achievable electric field in the magnetized thruster plasma. It has been shown that, without the SEE, the electron cross-filed transport reduces with the discharge voltage from anomalously high to nearly classical collisional level. This reduction may be associated with the shear of the electric field [61], [62]. For the considered $E \times B$ configuration of the thruster, the shear of the electric field can be exceptionally large when the electron emission from the wall is suppressed. Under such conditions, the magnetized thruster plasma can withstand much stronger electric fields than that with emitting walls. Overall, at high discharge voltages, the thruster discharge unaltered by the SEE can approach new regimes with significant electric field, pressure gradients, and supersonically rotating electrons. These high magnetic insulation regimes of the $E \times B$ thruster discharge require future kinetic studies.

In conclusion, for laboratory-magnetized plasmas, the use of nonemitting walls is essential in order to strengthen insulation properties of such plasmas. This is particularly relevant to plasma applications for which the control of the electric field is implemented with biased electrodes. Similar to this paper, the suppression of the SEE from, for example, the plasma-facing wall between the biased electrodes can be achieved using engineered materials such as carbon velvet [32], [53]. For the practical implementation of nonemitting walls, it is also important that this material is sputter resistant. The presented results and materials can be relevant to various plasma applications, which require the suppression of the SEE from the plasma-facing wall.

Appendix
Cross Sections for Elastic Electron–Xenon Atom Collisions Used in PIC Simulations

Simulations shown in Fig. 3 used the electrostatic direct-implicit PIC code [33] as in our previous simulations [34], [35], [45], [46] but with improved analytical approximations for differential cross sections for elastic scattering. The scattering of electrons in electron-neutral elastic collisions is characterized by the normalized differential cross section and the momentum-transfer collision cross section in the following forms:

$$\frac{\sigma_{sc}(E,\theta)}{\sigma_{sc}(E)} = \frac{1}{4\pi} \frac{1 - \xi^2(E)}{[1 - \xi(E)\cos\theta]^2} \tag{A1}$$

$$\frac{\sigma_m(E)}{\sigma_{sc}(E)} = \frac{1 - \xi(E)}{2\xi(E)^2} \left((1 + \xi(E)) \ln\frac{1 + \xi(E)}{1 - \xi(E)} - 2\xi(E) \right) \tag{A2}$$

where $\sigma_{sc}(E,\theta)$ is the differential cross section, $\sigma_{sc}(E)$ is the total cross section, $\sigma_m(E)$ is the momentum-transfer collision cross section, E is the electron energy in electronvolts, and θ is the angle of scattering relative to the initial direction of the electron velocity in the laboratory frame. Here, for the elastic scattering of electrons on xenon atoms at electron energies of $E < 1$ kV

$$\xi(E) = 0.9 + \frac{16.6 \left(\sin\left(4.8|\sqrt{E} - 0.673|^{0.43}\right) - 1.04 \right)}{E + 31.4}. \tag{A3}$$

References

[1] V. A. Rozhansky, A. A. Ushakov, and S. P. Voskboynikov, "Electric fields and currents in front of a biased electrode (flush mounted probe) and the I–V characteristics of the electrode for various mechanisms of transverse conductivity," *Nucl. Fusion*, vol. 39, no. 5, pp. 613–628, May 1999.

[2] S. J. Zweben, R. J. Maqueda, A. L. Roquemore, C. E. Bush, R. Kaita, R. J. Marsala, Y. Raitses, R. H. Cohen, and D. D. Ryutov, "Local scrape-off layer control using biased electrodes in NSTX," *Plasma Phys. Control. Fusion*, vol. 51, no. 10, p. 105012-36, Oct. 2009.

[3] D. D. Ryutov, "Mirror devices," *Plasma Devices Oper.*, vol. 1, no. 1, pp. 79–96, Dec. 1990.

[4] R. F. Ellis, A. Case, R. Elton, J. Ghosh, H. Griem, A. Hassam, R. Lunsford, S. Messer, and C. Teodorescu, "Steady supersonically rotating plasmas in the Maryland Centrifugal Experiment," *Phys. Plasmas*, vol. 12, no. 5, pp. 055704-1–055704-7, May 2005.

[5] A. J. Fetterman and N. J. Fisch, "Alpha channeling in rotating plasmas," *Phys. Rev. Lett.*, vol. 101, p. 20500, 2008.

[6] A. J. Fetterman and N. J. Fisch, "Wave-driven countercurrent plasma centrifuge," *Plasma Sources Sci. Technol.*, vol. 18, no. 4, p. 045003, Nov. 2009.

[7] M. Krishnan, M. Geva, and J. L. Hisrhfeld, "Plasma centrifuge," *Phys. Rev. Lett.*, vol. 46, no. 1, pp. 36–38, Jan. 1981.

[8] T. A. Carter and J. E. Maggs, "Modifications of turbulence and turbulent transport associated with a bias-induced confinement transition in the large plasma device," *Phys. Plasmas*, vol. 16, no. 1, pp. 012304-1–012304-10, Jan. 2009.

[9] Y. Raitses, L. A. Dorf, A. A. Litvak, and N. J. Fisch, "Plume reduction in segmented electrode Hall thruster," *J. Appl. Phys.*, vol. 88, no. 3, pp. 1263–1270, Aug. 2000.

[10] N. J. Fisch, Y. Raitses, L. A. Dorf, and A. A. Litvak, "Variable operation of Hall thruster with multiple segmented electrodes," *J. Appl. Phys.*, vol. 89, no. 4, pp. 2040–2046, Feb. 2001.

[11] A. Fruchtman and N. J. Fisch, "Variational principle for optimal accelerated neutralized flow," *Phys. Plasmas*, vol. 8, no. 1, pp. 56–58, Jan. 2001.

[12] A. Fruchtman, N. J. Fisch, and Y. Raitses, "Control of the electric-field profile in the Hall thruster," *Phys. Plasmas*, vol. 8, no. 3, pp. 1048–1056, Mar. 2001.

[13] Y. Raitses, M. Keidar, D. Staack, and N. J. Fisch, "Effects of segmented electrodes in Hall current plasma thrusters," *J. Appl. Phys.*, vol. 92, no. 9, pp. 4906–4911, Nov. 2002.

[14] P. C. Stangeby, *The Plasma Boundary of Magnetic Fusion Devices.* Bristol, U.K.: IOP, 2000, ser. Plasma Physics Series.

[15] N. Hershkowitz, "How does the potential get from A to B in a plasma?" *IEEE Trans. Plasma Sci.*, vol. 22, no. 1, pp. 11–21, Feb. 1994.

[16] Y. P. Raizer, *Gas-Discharge Physics.* New York: Springer-Verlag, 2001.

[17] G. S. Janes and R. S. Lowder, "Anomalous electron diffusion and ion acceleration in a low-density plasma," *Phys. Fluids*, vol. 9, no. 6, pp. 1115–1123, Jun. 1966.

[18] M. Keidar and I. I. Beilis, "Electron transport phenomena in plasma devices with $E \times B$ drift," *IEEE Trans. Plasma Sci.*, vol. 34, no. 3, pp. 804–814, Jun. 2006.

[19] G. R. Tynan, A. Fujisawa, and G. McKee, "A review of experimental drift turbulence studies," *Plasma Phys. Control. Fusion*, vol. 51, no. 11, p. 113001, Nov. 2009.

[20] A. Simon, "Ambipolar diffusion in a magnetic field," *Phys. Rev.*, vol. 98, no. 2, pp. 317–318, Apr. 1955.

[21] A. I. Morozov and V. V. Savelyev, *Review of Plasma Physics*, B. B. Kadomtsev and V. D. Shafranov, Eds. New York: Consultants Bureau, 2000, p. 203.

[22] S. Barral, K. Makowski, Z. Peradzynski, N. Gascon, and M. Dudeck, "Wall material effects in stationary plasma thrusters II. Near-wall and in-wall conductivity," *Phys. Plasmas*, vol. 10, no. 10, pp. 4137–4152, Oct. 2003.

[23] D. Staack, Y. Raitses, and N. J. Fisch, "Control of acceleration region in Hall thrusters," presented at the 28th Int. Electric Propulsion Conf., Toulouse, France, Mar., 2003, IEPC Paper 03-0273.

[24] A. Fruchtman, "Ambipolar and nonambipolar cross-field diffusions," *Plasma Sources Sci. Technol.*, vol. 18, no. 2, pp. 025033-1–025033-16, May 2009.

[25] E. Ahedo, J. M. Gallardo, and M. Martinez-Sanchez, "Effects of the radial plasma-wall interaction on the Hall thruster discharge," *Phys. Plasmas*, vol. 10, no. 8, pp. 3397–3409, Aug. 2003.

[26] I. Kaganovich, Y. Raitses, D. Sydorenko, and A. Smolyakov, "Kinetic effects in a Hall thruster discharge," *Phys. Plasmas*, vol. 14, no. 5, p. 057104, May 2007.

[27] M. Keidar, I. D. Boyd, and I. I. Beilis, "Plasma flow and plasma-wall transition in Hall thruster channel," *Phys. Plasmas*, vol. 8, no. 12, pp. 5315–5322, Dec. 2001.

[28] J. C. Adam, J. P. Boeuf, N. Dubuit, M. Dudeck, L. Garrigues, D. Gresillon, A. Heron, G. Hagelaar, V. Kulaev, N. Lemoine, S. Mazouffre, J. Perez-Luna, V. Pisarev, and S. Tsikata, "Physics, simulation, and diagnostics of Hall effect thrusters," *Plasma Phys. Control. Fusion*, vol. 50, no. 12, p. 124041, Dec. 2008.

[29] N. B. Meezan and M. A. Cappelli, "Kinetic study of wall collisions in a coaxial Hall discharge," *Phys. Rev. E, Stat. Phys. Plasmas Fluids Relat. Interdiscip. Top.*, vol. 66, no. 3, p. 036401, Sep. 2002.

[30] L. Garrigues, G. J. M. Hagelaar, J. Bareilles, C. Boniface, and J. P. Boeuf, "Model study of the influence of the magnetic field configuration and a performance and lifetime of a Hall thruster," *Phys. Plasmas*, vol. 10, no. 12, pp. 4886–4892, Dec. 2003.

[31] Y. Raitses, D. Staack, A. Smirnov, and N. J. Fisch, "Space charge saturated sheath regime and electron temperature saturation in Hall thrusters," *Phys. Plasmas*, vol. 12, no. 7, p. 073507, Jul. 2005.

[32] Y. Raitses, A. Smirnov, D. Staack, and N. J. Fisch, "Measurements of secondary electron emission effects in Hall thrusters," *Phys. Plasmas*, vol. 13, no. 1, pp. 014502-1–014502-4, Jan. 2006.

[33] D. Sydorenko, A. Smolyakov, I. Kaganovich, and Y. Raitses, "Modification of electron velocity distribution in bounded plasmas by secondary electron emission," *IEEE Trans. Plasma Sci.*, vol. 34, no. 3, pp. 815–824, Jun. 2006.

[34] D. Sydorenko, A. Smolyakov, I. Kaganovich, and Y. Raitses, "Effects of non-Maxwellian electron velocity distribution function on two-stream instability in low-pressure discharges," *Phys. Plasmas*, vol. 14, no. 1, p. 013508, Jan. 2007.

[35] D. Sydorenko, I. Kaganovich, Y. Raitses, and A. Smolyakov, "Breakdown of a space charge limited regime of a sheath in a weakly collisional plasma bounded by walls with secondary electron emission," *Phys. Rev. Lett.*, vol. 103, no. 14, pp. 145004-1–145004-4, Oct. 2009.

[36] F. Taccogna, R. Schneider, S. Longo, and M. Capitelli, "Modeling of surface-dominated plasmas: From electric thruster to negative ion source," *Rev. Sci. Instrum.*, vol. 79, no. 2, p. 02B903, Feb. 2008.

[37] E. Ahedo and F. I. Parra, "Partial trapping of secondary-electron emission in a Hall thruster plasma," *Phys. Plasmas*, vol. 12, no. 7, p. 073503, Jul. 2005.

[38] G. D. Hobbs and J. A. Wesson, "Heat flow through a Langmuir sheath in the presence of electron emission," *Plasma Phys.*, vol. 9, no. 1, pp. 85–87, 1967.

[39] H. Bruining, *Physics and Application of Secondary Electron Emission.* London, U.K.: Pergamon, 1954.

[40] Y. Raitses, D. Staack, M. Keidar, and N. J. Fisch, "Electron wall interaction in Hall thrusters," *Phys. Plasmas*, vol. 12, no. 5, p. 057104, May 2005.

[41] A. Dunaevsky, Y. Raitses, and N. J. Fisch, "Yield of secondary electron emission from ceramic materials of Hall thruster," *Phys. Plasmas*, vol. 10, pp. 2574–2577, 2003.

[42] L. D. Tsendin, "Energy distribution of electrons in a weakly ionized current-carrying plasma with transverse inhomogeneity," *Sov. Phys.— JETP*, vol. 39, p. 805, 1974.

[43] V. P. Pastukhov, "Classical longitudinal plasma losses from open adiabatic traps," in *Reviews of Plasma Physics*, B. B. Kadomtsev, Ed. New York: Consultants Bureau, 1987, p. 203.

[44] D. D. Ryutov, "Axial electron heat loss from mirror devices revisited," *Fusion Sci. Technol.*, vol. 47, no. 1T, pp. 148–154, Jan. 2005.

[45] D. Sydorenko, A. Smolyakov, I. Kaganovich, and Y. Raitses, "Plasma-sheath instability in Hall thrusters due to periodic modulation of the energy of secondary electrons in cyclotron motion," *Phys. Plasmas*, vol. 15, no. 5, p. 053506, May 2008.

[46] D. Sydorenko, A. Smolyakov, I. Kaganovich, and Y. Raitses, "Kinetic simulation of secondary electron emission effects in Hall thrusters," *Phys. Plasmas*, vol. 13, no. 1, pp. 014501-1–014501-4, Jan. 2006.

[47] A. A. Ivanov, A. A. Ivanov, Jr., and M. Bacal, "Effect of plasma–wall recombination on the conductivity in Hall thrusters," *Plasma Phys. Control. Fusion*, vol. 44, no. 8, pp. 1463–1470, Aug. 2002.

[48] S. Mizoshita, K. Shiraishi, N. Ohno, and S. Takamura, "Secondary electron emission from solid surface in an oblique magnetic field," *J. Nucl. Mater.*, vol. 220–222, pp. 488–492, Apr. 1995.

[49] Y. Raitses, J. Ashkenazy, G. Appelbaum, and M. Guelman, "Experimental investigation of the effect of channel material on Hall thruster characteristics," presented at the 25th Int. Electric Propulsion Conf., Cleveland, OH, Aug., 1997, IEPC Paper 97-056.

[50] N. Gascon, M. Dudeck, and S. Barral, "Wall material effects in stationary plasma thrusters I: Parametric studies of an SPT-100," *Phys. Plasmas*, vol. 10, no. 10, pp. 4123–4136, Oct. 2003.

[51] Y. Raitses, D. Staack, and N. J. Fisch, "Controlling the plasma potential distribution in segmented Hall thruster," *IEEE Trans. Plasma Sci.*, vol. 36, no. 4, pp. 1202–1203, Aug. 2008.

[52] W. Hargus and B. Pote, "Examination of a Hall thruster start transient," presented at the 38th Joint Propulsion Conf., Indianapolis, IN, 2002, AIAA Paper-2002-3956.

[53] Y. Raitses, D. Staack, A. Dunaevsky, and N. J. Fisch, "Operation of a segmented Hall thruster with low-sputtering carbon-velvet electrodes," *J. Appl. Phys.*, vol. 99, no. 3, p. 036103-1–036103-3, Feb. 2006.

[54] K. D. Diamant, J. E. Pollard, R. B. Cohen, Y. Raitses, and N. J. Fisch, "Segmented electrode Hall thruster," *Propul. Power*, vol. 22, no. 6, pp. 1396–1401, Nov. 2006.

[55] J. M. Haas and A. D. Gallimore, "Internal plasma potential profiles in a laboratory-model Hall thruster," *Phys. Plasmas*, vol. 8, no. 2, pp. 652–660, Feb. 2001.

[56] J. A. Linnell and A. D. Gallimore, "Internal plasma potential measurements of a Hall thruster using xenon and krypton propellant," *Phys. Plasmas*, vol. 13, no. 9, p. 093502, Sep. 2006.

[57] D. Staack, Y. Raitses, and N. J. Fisch, "Temperature gradient in Hall thrusters," *Appl. Phys. Lett.*, vol. 84, no. 16, pp. 3028–3030, Apr. 2004.

[58] D. Staack, Y. Raitses, and N. J. Fisch, "Shielded electrostatic probe for nonperturbing plasma measurements in Hall thrusters," *Rev. Sci. Instrum.*, vol. 75, no. 2, pp. 393–399, 2004.

[59] L. Dorf, Y. Raitses, and N. J. Fisch, "Electrostatic probe apparatus for measurements in the near-anode region of Hall thrusters," *Rev. Sci. Instrum.*, vol. 75, no. 5, pp. 1255–1260, 2004.

[60] E. Ahedo and D. Escobar, "Influence of design and operation parameters on Hall thruster performances," *J. Appl. Phys.*, vol. 96, no. 2, pp. 983–992, Jul. 2004.

[61] M. Cappelli, N. Meezan, and N. Gascon, "Transport physics in Hall thrusters," presented at the 40th Aerospace Science Meeting, Reno, NV, 2002, AIAA Paper-2002-0485.

[62] M. K. Scharfe, C. A. Thomas, D. B. Scharfe, N. Gascon, M. A. Cappelli, and E. Fernandez, "Shear-based model for electron transport in hybrid Hall thruster simulations," *IEEE Trans. Plasma Sci.*, vol. 36, no. 5, pp. 2058–2068, Oct. 2008.

[63] A. Litvak and N. J. Fisch, "Resistive instabilities in Hall current plasma discharge," *Phys. Plasmas*, vol. 8, no. 2, pp. 648–651, Feb. 2001.

[64] A. M. Kapulkin and V. F. Prisnyakov, presented at the 24th Int. Electric Propulsion Conf., Moscow, Russia, Sep. 11–15, 1995, IEPC Paper 95-3.

[65] A. A. Litvak and N. J. Fisch, "Rayleigh instability in Hall thrusters," *Phys. Plasmas*, vol. 11, no. 4, pp. 1379–1383, Apr. 2004.

[66] N. J. Fisch, A. Fetterman, Y. Raitses, A. Fruchtman, and J.-M. Rax, "Kinetic mechanisms of plume narrowing in a cylindrical Hall thruster," presented at the 44th AIAA Joint Propulsion Conf., Hartford, CT, Jul., 2008, AIAA Paper 2008-4997.

Dmytro Sydorenko received the Ph.D. degree in plasma physics from the University of Saskatchewan, Saskatoon, SK, Canada, in 2006.

He is currently a Postdoctoral Fellow with the University of Alberta, Edmonton, AB, Canada. His research interests include particle-in-cell simulation of plasmas of low-pressure discharges, and fluid and hybrid simulation of the earth's ionosphere and magnetosphere.

Yevgeny Raitses received the Ph.D. degree from the Technion–Israel Institute of Technology, Haifa, Israel, in 1997.

He is currently a Principal Research Physicist at the Princeton Plasma Physics Laboratory (PPPL), Princeton University, Princeton, NJ. He is currently a been with the PPPL since 1998, where he is leading research on plasma thrusters and related plasma technologies. Previously he held research positions at the Propulsion Physics Laboratory of Soreq NRC, Israel. His current research is focused on plasma-wall interactions in gas discharges, physics and applications of low temperature magnetized plasmas, plasma diagnostics, and plasma-based nanotechnology.

Dr. Raitses is a Fellow of American Physical Society and an Associate Fellow of American Institute of Aeronautics and Astronautics.

Nathaniel J. Fisch received the B.S., M.S., and Ph.D. degrees in electrical engineering and computer science from the Massachusetts Institute of Technology (MIT), Cambridge, in 1972, 1975, and 1978, respectively, where he was an MIT National Scholar.

He is currently a Professor of astrophysical sciences and the Director of the program in plasma physics, Princeton University, Princeton, NJ. He also is the Associate Director for Academic Affairs and the Head of the Hall Thruster Laboratory, Princeton Plasma Physics Laboratory, Princeton University. In addition to plasma thrusters and related plasma devices, his current research interests include plasma-based methods of generating extreme laser intensities and fusion concepts employing magnetically or inertially confined plasma.

Dr. Fisch is a recipient of the 2005 James Clerk Maxwell Prize of the American Physical Society, the Ernest Orlando Lawrence Award in 2004, the Department of Energy Bronze Medal for Outstanding Mentor in 2002, and the American Physical Society Award for Excellence in Plasma Physics in 1992. A Fellow of the American Physical Society and the National Aeronautics and Space Administration Institute for Advanced Concepts, he is also a recipient of a Guggenheim Fellowship in 1985.

Igor D. Kaganovich received the Ph.D. degree from St. Petersburg State Technical University, St. Petersburg, Russia, in 1992.

He held positions with the University of Houston, Houston, TX, the University of Antwerp, Antwerp, Belgium, and Ruhr University, Bochum, Germany. Since 2000, he has been a Member of the research staff, Princeton Plasma Physics Laboratory, Princeton University, Princeton, NJ, where he is currently a Principal Research Physicist. He serves as the Associate Director of the Department of Energy Plasma Science Center on Controlling Plasma Kinetics in low-temperature plasmas. He has authored more than 70 journal articles on the physics of intense beams, beam–plasma interactions, atomic physics, and low-temperature plasmas.

Dr. Kaganovich is a Fellow of the American Physical Society, cited for pioneering contributions to the kinetic modeling of plasmas, including collisionless electron heating, negative ion dynamics, Hall thrusters, and intense ion beam dynamics. He serves as a Senior Editor for the IEEE TRANSACTIONS ON PLASMA SCIENCE for "Basic Processes in Fully and Partially Ionized Plasmas." He was a recipient of an Alexander von Humboldt Fellowship in 1996.

Andrei Smolyakov received the M.S. degree in plasma physics and chemistry and the Candidate of Physical and Mathematical Sciences degree from Moscow Institute of Physics and Technology, Moscow, Russia, in 1983 and 1986, respectively.

From 1986 to 1992, he was with the Theoretical Division of the Department of Plasma Physics, Kurchatov Institute of Atomic Energy (currently the Institute for Nuclear Fusion, Russian Research Center "Kurchatov Institute") and with the Department of General Physics, Moscow Institute of Physics and Technology. Since 1992, he has been with the Department of Physics and Engineering Physics, University of Saskatchewan, Saskatoon, SK, Canada. His research interests include nonlinear plasma theory, magnetohydrodynamics, and transport phenomena in magnetically confined plasmas, waves, and instabilities in Hall plasmas.

Alexander Khrabrov is a Physicist with the Princeton Plasma Physics Laboratory, Princeton University, Princeton, NJ.